Additive manufacturing of biomimetic Titanium-Tantalum lattices for biomedical implant applications

Nicolas Soro [a],*, Erin G. Brodie [b], Abdalla Abdal-hay [c], Aya Q. Alali [c], Damon Kent [a], Matthew S. Dargusch [a]

[a] Centre for Advanced Materials Processing and Manufacturing (AMPAM), School of Mechanical and Mining Engineering, The University of Queensland, Brisbane, QLD 4072, Australia
[b] Department of Materials Science and Engineering, Monash University, Clayton, VIC 3800, Australia
[c] School of Dentistry, The University of Queensland, Herston Campus, 4072, Australia

HIGHLIGHTS

- Biomimetic titanium-tantalum bone scaffolds were successfully produced with a laser powder-bed fusion process.
- Morphological characteristics of the triply periodic minimal designs were retained through the manufacturing process.
- The compressive mechanical properties of the structures were found suitable for use as bone implant substitutes.
- In-vitro cell cultures demonstrated the excellent biocompatibility of these novel biomaterials and superiority of the interconnected open-pore designs.

GRAPHICAL ABSTRACT
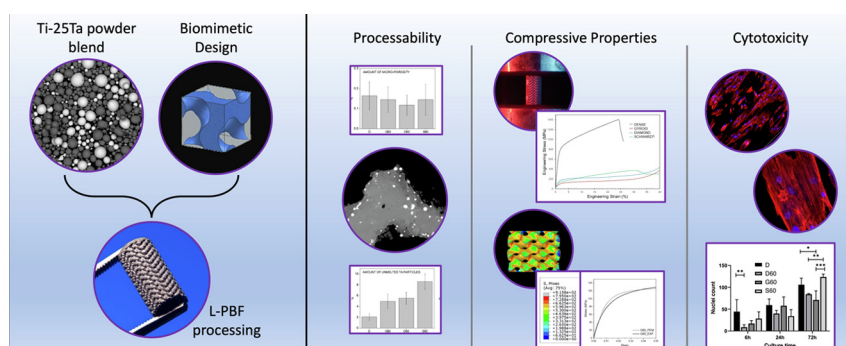
ARTICLE INFO

ABSTRACT

Although additively manufactured titanium-tantalum alloys can offer unique mechanical and biological advantages for implant applications, their use in conjunction with engineered lattice architectures is yet to be explored. In the present study, the promising gyroid, diamond and Schwarz primitive minimal surfaces are used for the design of 3D lattices for biomedical implants. The lattices are fabricated using laser powder-bed fusion and a blend of elemental titanium-tantalum powder. The processability, compressive mechanical properties and in vitro biological properties of the dense and lattice samples are assessed via non-destructive and destructive characterization methods. The topologies from the designed structures are retained through processing and the compressive tests results show that the strength-to-modulus ratios are comparable to the conventional Ti-6Al-4 V alloy. However, the higher ductility and absence of toxic elements make the Ti-25Ta lattices a more favourable option for a new generation of implants. Compared to conventional lattices, the designs presented here also show advantageous mechanical properties for use in bone implants with higher elastic admissible strains. The in vitro cell cultures confirm the high biocompatibility of the material and improved biological response of the interconnected lattices over dense material.

© 2022 The Authors. Published by Elsevier Ltd. This is an open access article under the CC BY-NC-ND license (http://creativecommons.org/licenses/by-nc-nd/4.0/).

---

* Corresponding author.
  E-mail address: n.soro@uq.edu.au (N. Soro).

1. Introduction

Additive manufacturing (AM) is emerging as a critical technology in the production of porous metallic biomaterials. The potential it affords to manufacture customized components with geometries not achievable through conventional approaches and with short lead times is a key factor in its adoption for fabrication of implants. In attempts to develop the ideal bone tissue analogue, extensive research has explored metallic biomaterials processed via laser powder-bed fusion (L-PBF) technologies [1–3]. The flexibility brought by powder-bed AM, in terms of feedstock material as well as geometric complexity, has shifted research efforts towards designing functional lattice structures that can meet mechanical and biological requirements for implants to replace bone. Among AM technologies, L-PBF is optimal for production of intricate internal architectures with small strut sizes (<200 µm) [4]. Given the recommended pore size for bone tissue engineering applications (i.e. 100–900 µm [5–7]), the L-PBF technology is amongst the most promising methods for fabrication of lattice implants to interface with bone [8–10]. L-PBF systems are also advantageous as they enable fabrication of alloys from elemental powder blends, so that investigations to assess the impacts of composition on their performance can be readily conducted – including for titanium-tantalum (Ti-Ta) alloys [11,12].

The Ti-6Al-4 V alloy is widely employed for load bearing medical implants owing to its excellent biocompatibility, superior mechanical properties and high corrosion resistance [13]. However, its relatively high elastic modulus can make implants mechanically incompatible with the surrounding bone, causing stress-shielding, which in the long term can lead to implant loosening and eventual failure [14,15]. In addition, there are concerns around aluminium (Al) and vanadium (V) used in Ti-6Al-4 V in regards to their toxicity when metallic ions are released in the patient's body [16,17]. Nontoxic, lower modulus Ti alloys have thus received great interest in the development of new metallic biomaterials [18,19].

The use of tantalum (Ta) as an alloying element for titanium alloys can address both of these limitations. Ta acts as a beta phase stabilizer in titanium (Ti) alloys, which substantially reduces the elastic modulus. In addition, Ta exhibits excellent biocompatibility and high corrosion resistance [20]. The bioactive properties of Ta have led to its use as a coating for Ti implants [21]. However, there have been limited attempts to use it as an alloying element for Ti at high concentrations. This may be attributed to its relatively high cost and density, and the difficulties associated with the conventional manufacture of Ta, primarily due to its very high melting point (3017 °C). Owing to the feedstock material flexibility and high energy input, AM technologies offer capability to economically process a wide variety of metals, including pure Ta [20,22] and Ti-Ta powder blends [12,23,24].

Although dense Ti-Ta alloys exhibit a reduced elastic modulus compared to more conventional alloys (i.e. Ti-6Al-4 V), the remaining mismatch in stiffness with surrounding bone tissue can still be detrimental for implant long-term reliability. Incorporating an interconnected porous network is an efficient means to further reduce the comparatively higher stiffness of metal implants, and to provide an anchor for enhanced cell attachment, cell growth and vascularization [25]. Additive manufacturing has enabled the tailoring of the mechanical and biological performances of biomedical implant through precise control over the morphological features of the lattices (i.e. pore shape, pore size, surface area) [26]. In addition to material selection, the design of optimized unit-cells has become an important aspect in the development of new biomaterials. For instance, previous work with a Ti-6Al-4 V alloy has highlighted the possibility to tailor the mass transport properties through architectural design inputs [27].

Given the great design freedom provided by AM processes, functional biomimetic lattices are attracting considerable interest in the design of bone implants. Triply periodic minimal surfaces (TPMS) have been used to create sheet-like structures [26] or skeletal structures [28] (also called ligament-based). These have advantages over conventional designs such as cubic, dodecahedron or octet-truss unit-cells in their biological properties, notably due to their higher permeability that can be correlated to their higher surface areas but also due to the lack of sharp features, which are detrimental for cell attachment [29]. Typically, these complex architectures also provide a better strength-to-weight ratio as well as higher elastic admissible strain (EAS), an important performance indicator in assessing a material's suitability for hard tissue engineering applications [30], defined by:

$$EAS = \frac{\sigma_{0.2\%}}{E} \times 100 \tag{1}$$

Where $\sigma_{0.2\%}$ is the yield strength at 0.2% offset and E is the Young's modulus.

Among titanium-tantalum alloys, previous investigations have reported that the Ti-25Ta and Ti-65Ta are the most suitable in terms of biomechanical compatibility with bones [31]. For these alloys, the elastic modulus typically falls in the range of 65–70 GPa, which is substantially lower compared to conventional Ti alloys and assists to minimize stress-shielding of the surrounding bone [15]. In previous work [31], the authors explored the two distinct compositions (i.e. Ti-25Ta and Ti-65Ta) and concluded that Ti-25Ta was preferable due to the alloy's reduced cost and lower density while the mechanical and biological properties were essentially identical for the two alloys. Thus, the Ti-25 Ta alloy was employed in the present study to further explore fabrication of lattice designs from elemental powders.

Most studies involving processing of titanium-tantalum powder blends with L-PBF have focused on producing dense materials, with a minimal amount of internal porosity [24,32]. Although fully dense material was achievable (>99.9%), a large proportion of un-melted Ta particles remain in the dense matrix. Fully melting the Ta particles has constituted the major challenge in the processing of Ti-Ta powder blends with L-PBF. Indeed, the significant difference in energy density required to melt both metals limits the range of suitable processing conditions. The high energy required to successfully melt Ta can be detrimental to obtaining fully dense material as it can lead to the formation of keyhole porosity [24]. Remelt scan strategies have been proposed to reduce the amount of remaining un-melted Ta particles and improve the material's chemical homogeneity, but these strategies have not been tested on TPMS lattice architectures.

In a recent work [23], we demonstrated the first use of L-PBF to produce lattices of different levels of porosity from the Ti-25Ta material with Schwarz unit-cells. Mechanical properties were suitable for bone implant applications, but surface irregularities were significant, and the overall processing and lattice designs required improvements. Based on these outcomes, further investigations into different lattice designs and optimized printing parameters are considered essential.

In the present study, we expand the use of the new Ti-25Ta alloy to a new promising set of TPMS lattice geometries, building on previous studies [23,24,31,32]. Using a constant 60% porosity, we designed and manufactured gyroid, diamond and Schwarz primitive lattices using L-PBF for the first time. The processability, mechanical properties and cytotoxicity of the fabricated Ti-25Ta samples are assessed and discussed in the context of implantable bone devices.

2. Materials and methods

2.1. Powder morphology and preparation

The feedstock material used for the fabrication of the metallic lattices was a powder blend made of 75 wt% commercially pure titanium (CpTi) and 25 wt% tantalum (Ta). The blend was tumble mixed for 12hrs at 15 rpm to obtain high powder homogeneity. The characteristics of both the titanium and tantalum powders are presented in Table 1 and the SEM image in Fig. 1 shows the Ti-25Ta powder blend used for the fabrication of the samples. Fig. 1 notably shows that bimodal powder distribution is obtained with this blend, with a median size of 3.39 µm for the CpTi and 7.18 µm for the Ta. Although bimodal powder blends can provide a better packing density, it is mostly agreed in the literature that there is no difference in final density for LBPF-produced parts when using bimodal powder blends compared to monomodal powder [33,34].

Both dense specimens and lattices have been successfully produced in prior work using L-PBF technology and an identical Ti-25Ta elemental powder blend [23,24].

2.2. Design of lattices

In addition to dense specimens, three types of lattices were fabricated with the Ti-25Ta material. The computer-aided design (CAD) models for the lattices were generated using the equation-based modeller Mathmod by repeating a single cell from a triply periodic minimal surface (TPMS) equation in three dimensions (cf. Fig. 2. and Table 2.). The gyroid, diamond and Schwarz primitive unit-cell types were selected, and their equations are presented below. L-PBF fabrication of all three geometries has shown great potential for biomedical applications in terms of biological and mechanical performances [35]. A 60% level of porosity was chosen on the basis of our previous work with Schwarz lattices and the Ti-25Ta alloy [23] to attain mechanical requirements for cortical bone replacements.

$$F_G(x, y, z) = \cos(x)\sin(y) + \cos(y)\sin(z) + \cos(z)\sin(x) + K \quad (2)$$

$$F_D(x, y, z) = \sin(x)\sin(y)\sin(z) + \sin(x)\cos(y)\cos(z)$$
$$+ \cos(x)\sin(y)\cos(z) + \cos(x)\cos(y)\sin(z) + K \quad (3)$$

$$F_S(x, y, z) = \cos(x) + \cos(y) + \cos(z) + K \quad (4)$$

2.3. Fabrication via laser powder bed fusion (L-PBF)

The dense and lattice Ti-25Ta samples were manufactured using laser powder bed fusion (L-PBF) on a Concept Laser MLab Cusing machine. The printing process was conducted under an argon atmosphere to ensure that oxygen content was kept below 0.2%. A 1 mm solid base plate was added for fabrication of the specimens to allow for cutting and removal of the specimens from the build platform using wire electrical discharge machining (EDM). Preliminary optimizations of the parameters were conducted

Table 1
Powder properties provided by suppliers.

Powder type	Titanium (CpTi)	Tantalum (Ta)
Provider	TLS Technik	Tekna
Production technique	Argon atomization	Plasma Spheroidization
Particle shape	Spherical	Spherical
Particles size	20 – 45 µm	15 – 45 µm
	< 10% above 39 µm	< 3% above 45 µm
	> 90% below 39 µm	> 97% below 45 µm

specifically to obtain dense material with minimal amounts of unmelted Ta particles and minimal internal micro-porosity within the struts. Further information can be found on this optimization in the cited work [24]. The L-PBF processing parameters employed for this work are presented in Table 3.

2.4. Micro-computed tomography (µCT) and scanning electron microscopy (SEM)

All specimens were cleaned in an ultrasonic bath of acetone for 15 min and then rinsed with ethanol to remove loose powder particles from the surface and inside the porous network.

To assess the lattice processability of the Ti-25Ta material with L-PBF, micro-computed tomography (µCT) scans were conducted for the three types of lattices using a Bruker Skyscan 1272. Due to the high density of the Ti-25Ta material and the scanner's technical limitations (i.e. maximum voltage of 100 kV), the specimens had to be machined down from 6 mm to 3 mm in diameter to ensure that the X-Rays could penetrate the specimens. The optimized µCT scanning parameters are presented in Table 4. A volume of interest (VOI) of 2 mm³ for each CT scan was used for the measurements of surface area, volume, strut thickness and pore size using Fiji software. It should be noted that prior to the measurement of surface areas specifically, the outer surfaces delimiting the VOI were removed to ensure only the TPMS geometry was taken into account. The maximal pore sizes were calculated using the trabecular spacing (Tb.Sp) calculation within BoneJ module. The algorithm defines Tb.Sp as the diameter of the largest sphere that can fit within the void domain at any point [36]. Because the local surface irregularities impacted the automated measurement of strut size, the minimal strut sizes had to be manually measured within the 3D µCT reconstructed data.

Dense specimens and lattices were sectioned and ground with SiC paper (grit 320 to 4000) in both transverse and longitudinal directions to be observed under a Hitachi TM3030 scanning electron microscope (SEM). The SEM images were used to assess the proportion of unmelted Ta particles remaining, their distribution and the distribution of internal micro-porosity within the fabricated material. These were obtained using the thresholding tools within Fiji software. All reported values for %Ta remaining and % porosity were averaged from 10 measurements on randomly ground sections both along the building direction and transversal to the building direction.

2.5. Compressive mechanical testing

The specimens were machined down to 11 mm in height using EDM, ensuring both end surfaces were parallel. Using an Instron universal testing machine, uni-axial compressive tests were conducted on the 3 lattice types and dense specimens according to the ASTM E9 standards. The crosshead speed was kept constant at 0.003 mm/s and the scan rate was set to 1 data point every 0.02 s. The compressive strains were measured using an advanced video extensometer (AVE) system, which allowed tracking two painted dots on the specimens. The gauge lengths were between 5.8 mm and 6.2 mm and compression tests were conducted at least three times for each group. The stress was extracted from the load-cell measurement (100 kN load-cell), and stress–strain curves were plotted considering the global stress (σ) as the force (F) reported to the entire cylindrical section of the specimens (A) as follows:

$$\sigma = \frac{F}{A} = \frac{F}{\pi 6^2} \quad (5)$$

Through this study, the compression moduli of the lattice structures are referred as "elastic moduli" or "Young's moduli". In contrast to the Young's modulus of a bulk material, the Young's
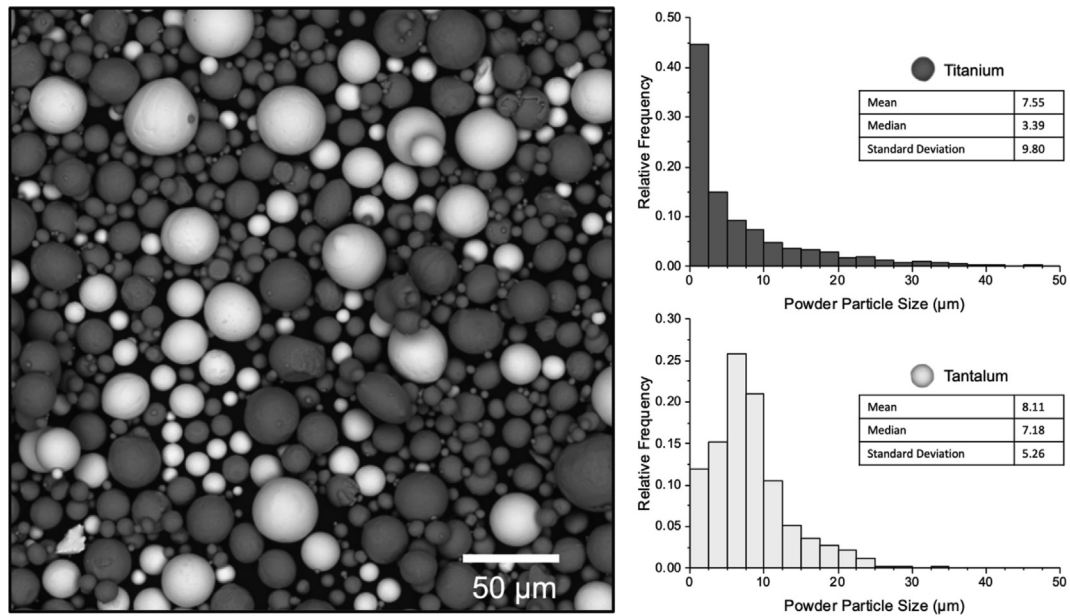
Fig. 1. Powder mixture and powder size distribution of the Ti-25Ta used for the fabrication of the samples with L-PBF. Ti particles are dark grey and Ta particles are light grey.
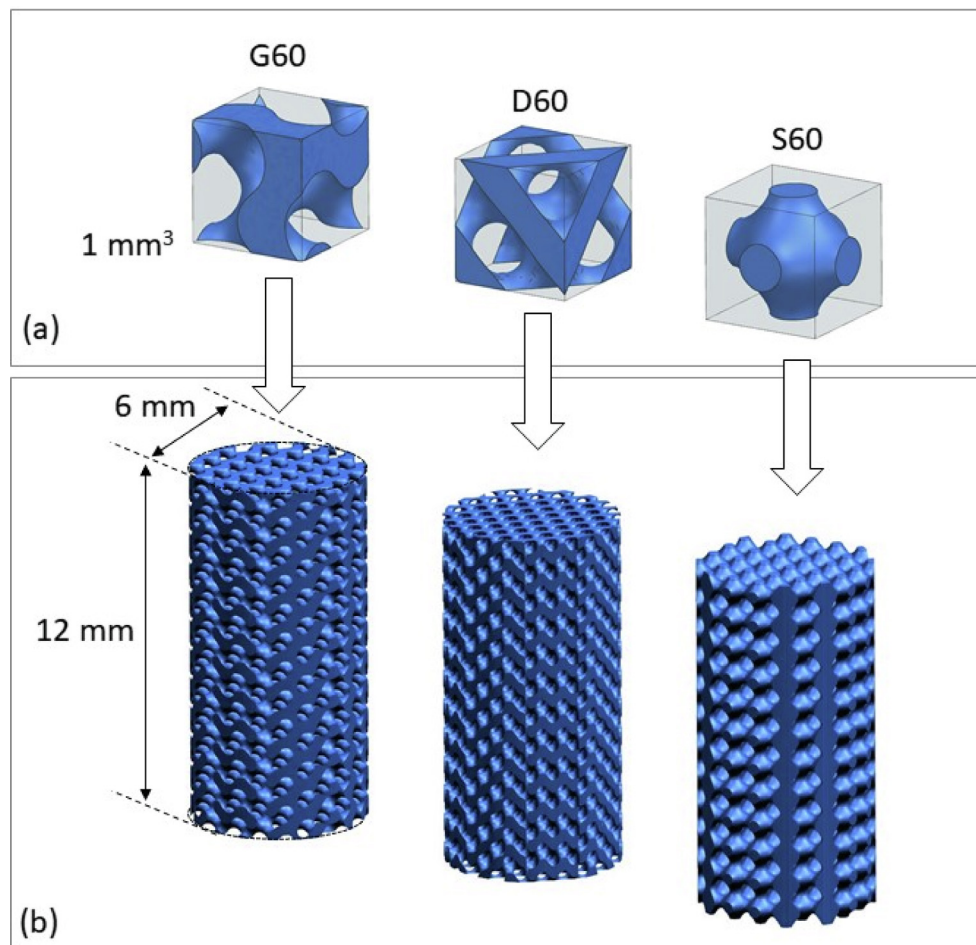

Fig. 2. Dimensions and characteristics of (a) the unit-cells and (b) the full-size CAD models used for the L-PBF prints.

modulus reported for lattices is directly dependant on the morphological parameters of the structure (i.e. pore size and shape), in addition to its inherent material's properties. Using the same terminology for bulk material and lattices allows for a direct comparison and provide clear insights into the effect of the lattice network on the stiffness of the structures.

Table 2

Morphological characteristics of the CAD models for the skeletal-based TPMS and dense material.

Group ref.	Sample type	K (Eq. Offset)	Level of porosity (%)	Size of unit-cells d (mm)	Sample diameter (mm)	Sample height (mm)
D	Dense material	N/A	0	N/A	6	12
G60	Gyroid lattices	0.3	60	1	6	12
D60	Diamond lattices	0.25	60	1	6	12
S60	Schwarz p. lattices	0.4	60	1	6	12

Table 3

Scanning parameters used for the L-PBF processing of TPMS lattices.

Parameter	Dense Sample (group D)	Lattice Samples (groups G60, D60 and S60)
Laser Power (P)	95 W	95 W
Layer thickness (t)	25 μm	25 μm
Hatch distance (h)	35 μm	35 μm
Scanning speed (v)	300 mm/s	600 mm/s

Table 4

μCT scanning parameters.

Parameter	Value
Exposure time	2600 ms
Voltage X-ray	100 kV
Current X-ray	100 μA
Rotation step	0.45°
Averaging	4 frames
Energy filter	Cu 0.11 mm
Pixel size (resolution)	9 μm
Image format	1224 × 820

It should be noted that due to the substantial "pancake" deformations endured with the Ti-25Ta alloy due to its high ductility, the AVE system eventually lost track of the dots for almost all test specimens. Because this happened late during the test and well after yielding of the material (i.e. tracking was lost after 30%-50% strain), it did not affect the calculation of elastic properties.

2.6. Finite element analysis (FEA)

Finite element (FE) models were generated for comparison to the experimentally determined mechanical performance. The predictions from the FE models were used to give further insights into the processability of the lattices. An elasto-plastic material behavior was extracted from the uni-axial compression experimental testing of the dense Ti-25Ta specimens and input into ABAQUS [37]. Reduced structures of $3 \times 3 \times 3$ unit-cells were used in order to decrease computation time, while still being mechanically representative of the full lattice structures [38,39]. The models were generated using the Equations 2–4 in Mathmod, exported in OBJ format and meshed with 3D linear tetrahedral elements using Salome open-source software with an average element size of 30 μm.

2.7. Cytocompatibility assessment

Cell attachment and proliferation on the fabricated samples were investigated using osteoblasts cells by the direct seeding method. The fabricated samples were cut into 2 mm thick discs with a precision cutter, which represented 2 rows of unit-cells in thickness. Subsequently, the samples were ground with SiC paper (1200, 2500 and 4000 grit) and sonicated for 5 mins in water and ethanol (50%-50%). The cleaned samples were sterilized in ethanol for 1 h and kept inside a biosafety cabinet for 24 h to allow full removal of ethanol from the scaffolds. Alveolar-bone derived osteoblasts cells were extracted from human teeth (as previously reported [40]) and cultured in Dulbecco's modified Eagle's α-minimum essential medium (α-MEM; Gibco®, Life Technologies, Australia), which contains 20% fetal bovine serum (FBS; In Vitro technologies, Australia) and 1 vol% penicillin/streptomycin (P/S; Gibco®, Life Technologies, Australia). The cells were incubated at 37 °C in a 95% humidified atmosphere of 5% CO_2 and the culture medium was changed every 2–3 days. Once the cultured cells reached a 90% confluence, they were exposed to 0.25% trypsin for 3 min (containing 1 mM EDTA, Gibco®, Life Technologies, Australia).

The Ti-25Ta specimens were exposed to UV light for 30 min on each side before the immersion in the α-MEM. Specimens were immersed in the culture medium for 2 h to reach stability and enhance seeding efficiency. The primary osteoblast cells were directly seeded with a density of 3×10^3 cells per well, in a 48-well plate. The seeded samples were incubated for 30 min before adding the α-MEM to enhance cell attachment to the sample surface. Subsequently, the samples were transferred to a new 48-well plate and the α-MEM media was added until the samples were fully covered.

AlamarBlue ™ quantification assays were used to evaluate the metabolic activity and DNA quantification was used to measure the proliferation of the osteoblasts. According to the manufacturer's protocol, cell metabolism was measured at 6 h, 24 h and 72 h. The culture medium was replaced with 300 μl of medium containing 10 vol% of AlamarBlue solution and the cells were incubated at 37 °C for 4 h. The fluorescence method was used to assess the percentage of reduction with an excitation wavelength of 560 nm. Using a spectrofluorometer (POLARstar Omega, BMG Labtech, Germany) and a wavelength of 590 nm, the emitted fluorescence was obtained. A PicoGreen™ DNA quantification assay (P11496, Invitrogen, Australia) was conducted according to manufacturer's methods. The cultured cells were washed in PBS and frozen at −80 °C on day 1, 3 and 5, until further processing. Using a Tris-EDTA buffered solution with Proteinase-K (0.5 mg/ml), the cells were digested overnight at 56 °C. The DNA content was assessed using a spectrofluorometer, as described in previous work [41].

At the specific time points of Day 1 and Day 5, the cell morphology was visualized using 4,6-diamino-2-phenylindole (DAPI, Life Technologies, NY, USA) and Alexa Fluor 568 Phalloidin (Life Technologies, Grand Island, NY, USA). The samples were cleaned using PBS and fixed for 20 min in 4% Paraformaldehyde. The samples were then incubated for 5 min with 0.5% Triton-X100 for membrane permeabilization, cleaned in PBS and incubated for 30 min in a solution containing PBS, 5 μg/ml DAPI and 0.8U/ml Alexa Fluor 568 Phalloidin, for membrane permeabilization.

Data reported from the cell culture analysis are expressed as mean ± standard deviation. Analysis of variance was conducted to compare the groups (one-way ANOVA and Tukey's test). Prism 9.0 software was used for statistical analysis, and a p value < 0.05 was considered statistically significant.

3. Results & discussion

3.1. Processability of Ti-25Ta lattices with L-PBF

The dense, gyroid, diamond and Schwarz primitive samples were successfully manufactured from the elemental Ti-25Ta powder blend using laser powder bed fusion. A macrograph of the printed lattices is presented in Fig. 3. To assess the processability of dense specimens and the TPMS lattice designs from the Ti-25Ta material using L-PBF, morphological and microstructural observations were conducted. The compressive mechanical properties and cell culture analysis are discussed separately in the next sections.

As reported in Table 5, the measured porosities, maximal pore sizes and minimal strut sizes show variance compared to the designed porosity. This is an expected outcome with L-PBF and can be explained by the physics of the melt pool that result in semi-melted powder particles adhering to the surface of the lattice that inherently increase the struts' size and SA:V ratios [42,43]. While the topologies from the TPMS equations were retained through L-PBF processing (Fig. 4), the resulting surface roughness and irregularities are clearly visible in the reconstructed data from µCT scans presented. The mismatch in measured porosity is much higher for the D60 group compared to the G60 and S60 groups, with respective discrepancies of 29.3%, 11.5% and 10.1%. This can be attributed to smaller pore sizes and strut sizes for the diamond lattices, which means an identical increase in strut size will have a larger relative influence on the level of porosity. In fact, the three geometries presented consistent mismatches in terms of strut sizes, measured at 105 µm, 103 µm and 116 µm for the gyroid, diamond and Schwarz respectively. These variations are in agreement with previous published studies with L-PBF [10,23,43]. However, standard deviation for the minimal strut size was found much higher for the Schwarz than the two other lattice groups. This can be associated to the presence of both vertical struts with small variations and horizontal struts with larger variations (due to the overhang nature) in the Schwarz lattices. These variations are less apparent with the measurements of inclined struts in the diamond and gyroid lattices.

In terms of processability of lattices with this powder blend, the tomography data show that designed pores that are too small (i.e. 400 µm and below) can be problematic, as significant excess powder bonding may obstruct pores, which can be detrimental to obtaining a fully interconnected porous network for the targeted bone implants applications.

As identified in the introduction, a major challenge in the L-PBF fabrication of elemental Ti-Ta powder lies in supplying sufficient energy to fully melt the Ta particles without exposing the Ti particles to excessive energy leading to defects during processing. This results in unmelted Ta particles within the dense matrix after solidification of the material. For dense material, this phenomenon was investigated in previous work [24], and the authors attributed the scanning speed of the laser to be the major contributing factor to the amount of remnant tantalum particles. In that study, the proportion of unmelted Ta was measured to be between ∼ 0.25 – 2.75% depending on the scan speed (varying between 100 and 700 mm/s). In the present work, a percentage of 2.1% ± 0.6 of unmelted Ta was measured from SEM images in the dense specimens, agreeing with the most recent work which calculated an unmelted Ta particle percentage of 2.07% ± 0.01 from µCT at identical scanning conditions [32]. Brodie et al. [24] also investigated a remelt scan strategy that was successful in reducing the amount of unmelted Ta particles within the matrix. It was found that for single scan strategies, lower scan speeds could reduce the amount of unmelted Ta particles though to the detriment of an increased internal porosity. However, increasing the energy density by lowering the scan speed could also result in excessive energy absorption in Ti particles leading to keyhole porosity.

While not investigated in prior work, the proportion of unmelted Ta in the current TPMS lattices was significantly higher than what is reported for bulk Ti-25Ta [24], with up to 7.8% in volume for the Schwarz lattice specimens (cf. Fig. 5). Compared to a bulk structure, thin struts are exposed to less heat during the L-PBF processing, which lowers the energy density and increases the likelihood for unmelted Ta. The difference in scan speed from 300 mm/s to 600 mm/s between the dense Ti-25Ta and Ti-25Ta lattices – and thus energy density provided – is also most likely a contributing factor.

Although it is likely that the reductions in heat and energy density during fabrication of the lattices, compared to the dense material, may hinder melting of Ta, the discrepancies observed between the three geometries are ambiguous. As presented in Fig. 5.a, the highest amount of unmelted Ta was measured in the S60 specimens, despite the D60 having the thinnest struts. This suggests that the laser path during L-PBF, which is related to unit-cell topology, may influence the amount of unmelted Ta particles and also leads to their heterogeneous distribution within the lattices, as shown in Fig. 5.d-f. In general, there is a higher density of unmelted Ta at the extremities of the struts than in the interiors, which can be related to reduced heat exposure in near-surface regions.

Further details regarding the microstructural features and composition of the Ti-25Ta alloy can be found in previous publications [23,24], in which transmission electron microscopy (TEM), scanning electron microscopy (SEM), X-ray spectroscopy (EDS) and electron backscattered diffraction (EBSD) analyses were used to assess the grain structure and compositional homogeneity.

According to previous studies, a bimodal distribution (as observed with the Ti-25Ta powder in the present work. cf. Fig. 1)
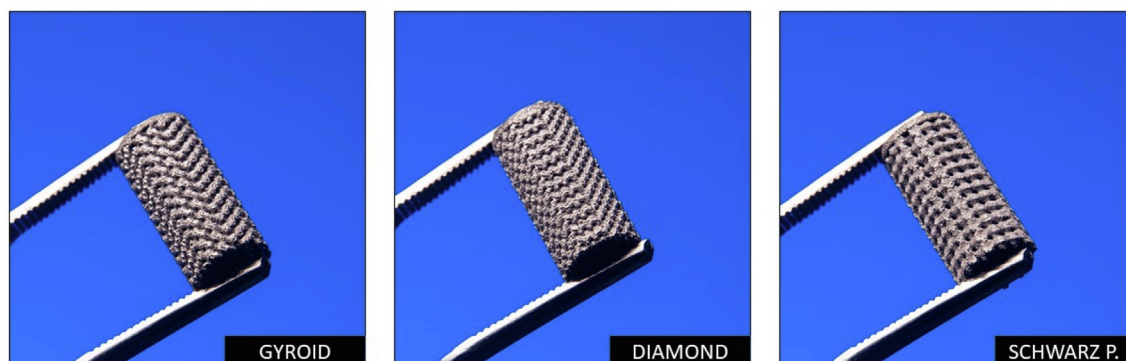

Fig. 3. Macrographs of Ti-25Ta lattices produced using L-PBF. Note that the base plate, visible on the top side in these images, was removed for mechanical testing.

Table 5
Main morphological characteristics of lattices from CAD models and μCT scans.

Group reference	Level of porosity [a] (%)	SA:V Ratio	Max pore size (μm)	Min strut size (μm)
G60$_{CAD}$	60	7.5	520	400
G60$_{CT}$	48.5 ± 1.3	11.52 ± 0.92	429 ± 15	505 ± 16.4
D60$_{CAD}$	60	9.4	400	300
D60$_{CT}$	30.7 ± 2.4	8.85 ± 0.30	276 ± 17	403 ± 18
S60$_{CAD}$	60	5.68	950	330
S60$_{CT}$	49.9 ± 0.9	8.93 ± 0.52	700 ± 16	446 ± 33

[a] The level of porosity does not account for the micro porosity brought about by the manufacturing process.

should not affect the density of the final LPBF parts [33,34]. However, given the significant mismatch in density and melting point between the two metals used in the present work, other physical phenomena may be involved during processing, which may hinder the melting of the Ta particles. It is suggested that further investigations be conducted to assess the effect of Ti and Ta powder size on densification of the Ti-Ta matrix and melting of Ta.

3.2. Compressive mechanical properties

The stress–strain curves from the compression tests are presented in Fig. 6 and resulting mechanical properties presented in Table 6. As the data from the compressive tests were consistent and repeatable, only one representative curve for each sample type is shown. The repeatability can also be supported by the relatively low standard deviations from the extracted mechanical properties, as reported in Table 6.

The dense Ti-25Ta material presented a Young's modulus of 70.3 GPa, which is comparable to what was previously reported with an identical alloy composition (i.e. 73.5 GPa in [23] and 65 GPa in [24]). Compared to the industry standard Ti-6Al-4 V, this represents a reduction in modulus of 36%, which is desirable for an alloy targeted toward bone implant applications. With the addition of the interconnected porous networks to this titanium-tantalum material, the elastic moduli are reduced to the range of 10.4–18.9 GPa, depending on the lattice's unit-cell geometry. This represents a suitable range of moduli for use in cortical bone implant applications [6].

The compressive response of the gyroid and diamond lattices was characterized by 4-stages: (1) elastic phase, (2) yielding, (3) hardening and (4) densification, which is typical for ductile materials [23,44]. However, the S60 group showed a different mechanical behavior with no densification stage as the structure was subject to buckling from ∼ 30% strain, indicated by a reduction in the stress at this point in the compression. The gyroid lattice showed the lowest Young's modulus of 10.4 ± 1.5 GPa and corresponding lowest yield strength of 74 ± 4 MPa. The diamond lattices exhibited the middle Young's modulus of 15.8 ± 0.5 GPa but the highest yield strength of 126 ± 11 MPa, outperforming the Schwarz lattices yield strength by approximately 20 MPa. The relatively high elastic modulus of 18.9 ± 2 GPa observed for the Schwarz group can be explained by the presence of vertical struts that provide direct support for the uni-axial loading. In terms of EAS, the diamond group presented the highest EAS of 0.80%, followed by the gyroid (0.72%) and the Schwarz (0.54%). Both gyroid and diamond lattices are bending-dominated structures with inclined struts at 45°, which explains the similar mechanical responses and similar EAS reported. The more significant reduction in EAS for the Schwarz group can likely be explained from the buckling of the structure discussed in the following paragraph.

From about 25% strain, densification occurred for the gyroid and diamond lattices until the specimens were almost completely flattened (i.e. 70% strain). This is evident from the smooth increase in stress in the curves as the pores close and the struts come into con-

tact with each other at higher strains [44]. The Schwarz lattices withstood higher stresses after yielding and before the densification occurred, compared to the other two lattice structures. The buckling behavior observed in the Schwarz p. geometry is typical for stretching-dominated structures [45] and can be explained by the lack of resistance to bending load induced by thinner struts aligned to the loading direction [46]. In a study from Nazir et al. [47], the authors concluded that horizontal or inclined struts provide support to bear the buckling loads. Here, the Schwarz lattice does not possess inclined struts and is susceptible to buckling. The authors also concluded that having a denser structure as far from the central axis as possible can increase buckling resistance. Although incorporating a gradient in density could potentially alleviate the buckling of the S60 design, this would be less desirable for the targeted bone implant applications, as a highly porous structure is preferred to provide a suitable anchor for bone in-growth and to reduce the elastic modulus [48]. Structures that are subject to buckling would not be desirable for load-bearing implant applications, as this causes instability and unpredictability in the mechanical response.

After significant deformation (i.e. 22–42% strain), the dense specimens failed following a mixed mode of ductile and brittle fracture mechanisms, characterized by dimple tearing and cleavage areas on the fracture surfaces, also observed by Atee et al. in a Ti-6Al-4 V alloy [49]. The final fracture of the dense specimens occurred along a 45° plane to the loading direction. More details on the fractography of the dense specimens that exhibited similar fracture modes are provided in prior work [24].

It should be noted that in some of our previous work with the same Ti-25Ta alloy [23], the dense specimens did not fracture and presented a higher ductility, with global strain reaching above 70%. A chemical analysis from ICP-AES has shown slight variations in the material's chemical composition over time since this first batch, notably due to the difference in Ta content in the powder blend. Nevertheless, the compression data emphasized the high ductility of the Ti-25Ta alloy through the gyroid and diamond groups. These two groups did not exhibit a clear fracture, and tests were stopped after 70% strain, as significant densification was apparent at this stage. For the gyroid and diamond groups that showed a densification stage after hardening without clear failure, the UCS were measured at the densification inflection point, in the same way to what was presented in previous work [50,51]. Compared to the conventional Ti-6Al-4 V, the high ductility of the Ti-25Ta alloy prevents the lattices from failing abruptly with successive struts' factures. For bone implant applications, this ductile mode of failure from the Ti-25Ta is more favourable, as the lattices can maintain some level of structural integrity and functionality before a replacement is implanted.

To assess the biomechanical compatibility of an implant material with bone, the elastic admissible strain (EAS) is preferred over the elastic modulus or yield strength independently. The EAS is defined by the ratio of the yield strength over the Young's modulus and is a good indicator of a material's mechanical suitability for hard tissue engineering application. As presented in Table 6, the
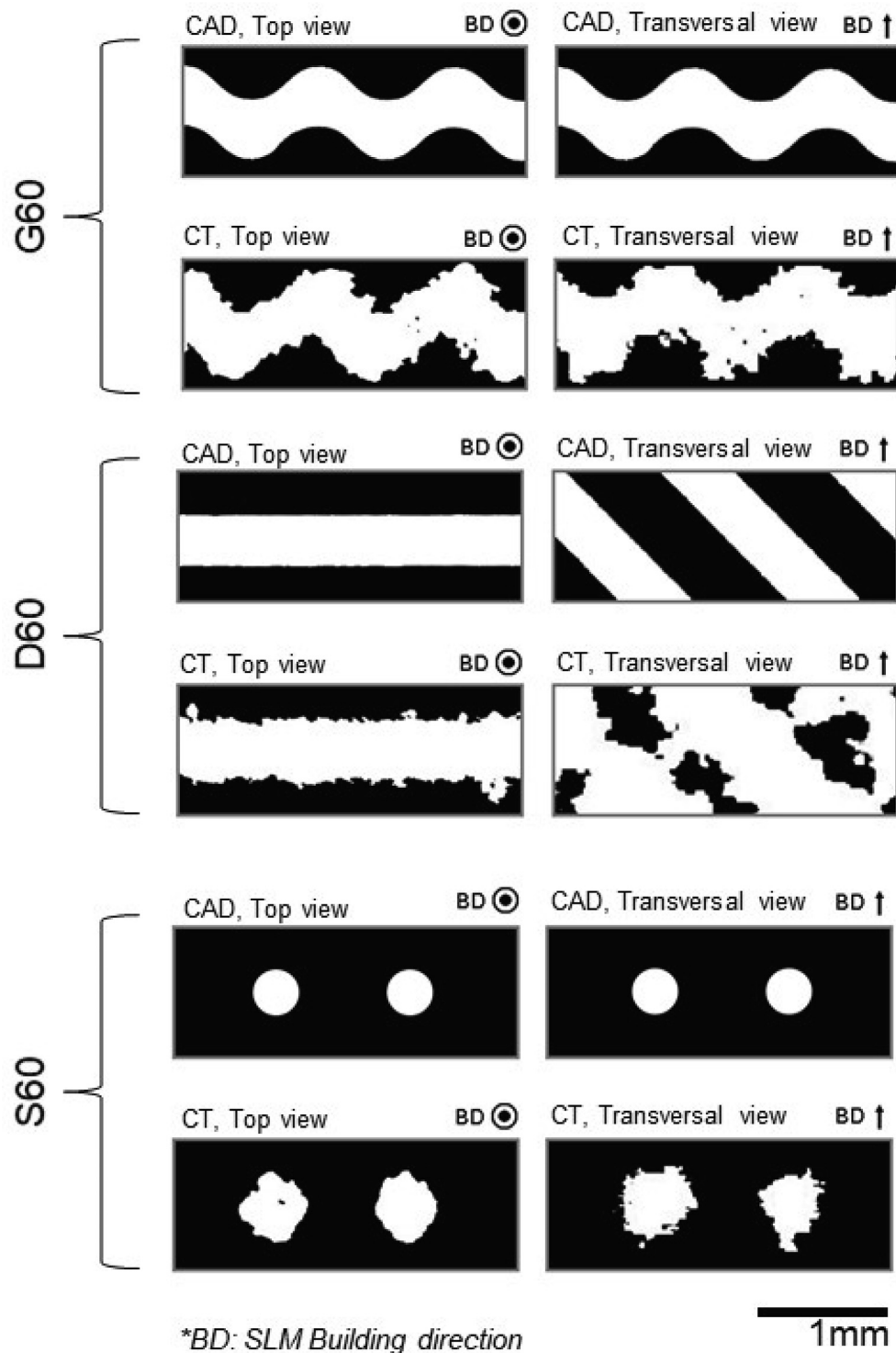
Fig. 4. Comparison between sectioned CAD files and slices extracted from μCT reconstructed data. White areas represent material while black areas represent void. The figure shows the surface irregularities and discrepancies of the fabricated specimens brought about by the L-PBF process.

dense Ti-25Ta has an EAS of 0.97% compared to 0.84% in our previous work [23], which represents a 15% increase. This increase in EAS can be directly associated to the increase in yield strengths from the new batch, which can be attributed to the slight variations in chemical compositions between the two prints. In contrast to dense material, lattices generally exhibit lower EAS values due to geometric stress concentrators [43], which act to reduce the relative strength as confirmed by the current results. Compared to

recent work with Ti-25Ta F_2CC_z lattices [52], the TPMS used in the present study showed higher ductility with no successive struts failures and similar strengths. However, the EAS from the F_2CC_z lattices were found significantly higher (3.48%). Previous studies have reported that with porous materials or lattices, the rate at which the elastic modulus decreases when increasing the level of porosity is higher than the rate at which the yield strength decreases [53,54]. Thus, it can be expected that, at high levels of
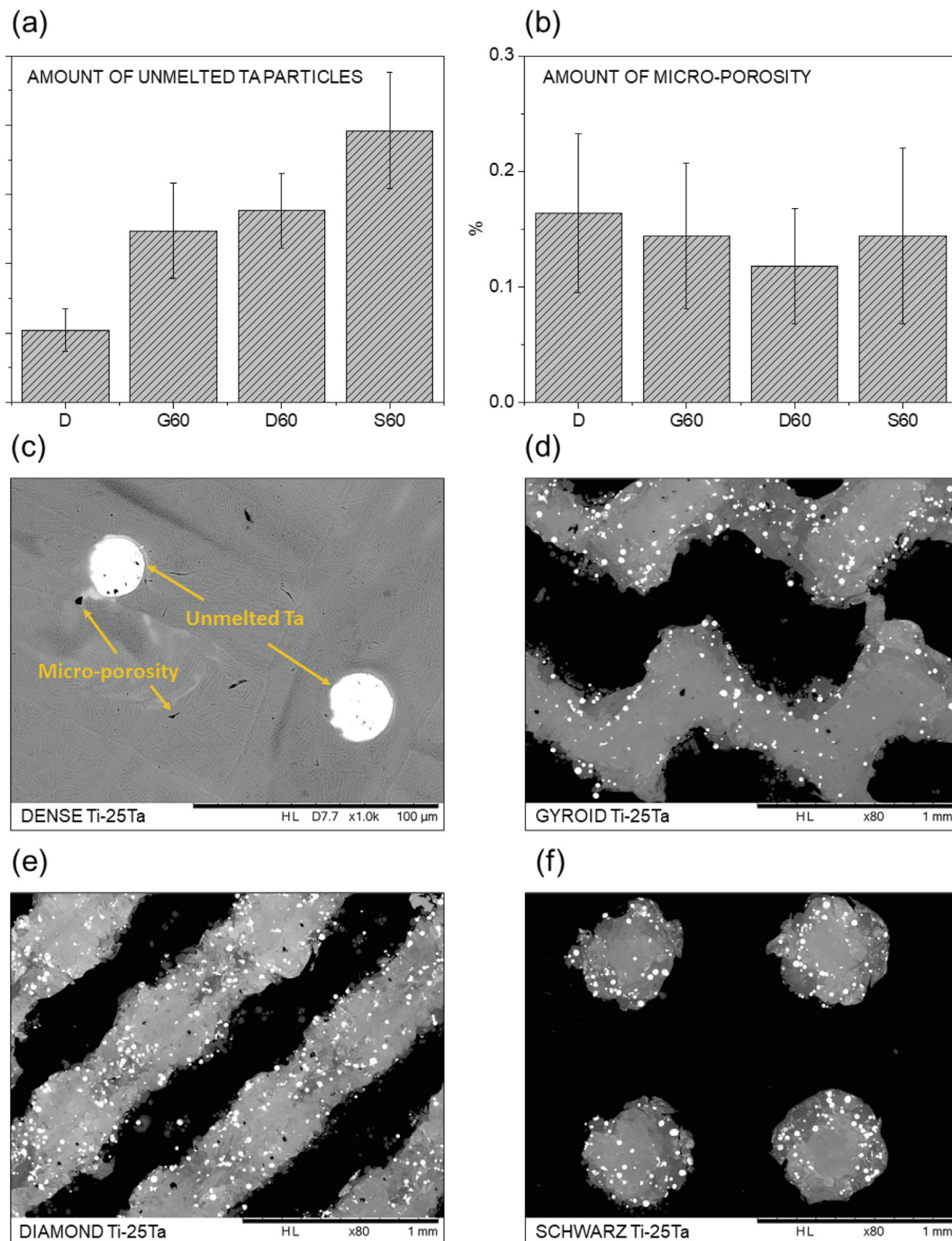
Fig. 5. Unmelted tantalum powder particles and micro-porosity in the Ti-25Ta specimens. (a) Bar chart showing the relative amount of unmelted Ta particles for dense and lattice Ti-25Ta specimens, (b) Bar chart showing the relative amount of micro-porosity for dense and lattice Ti-25Ta specimens, and (c), (d), (e) and (f) respectively showing SEM images of the dense, gyroid, diamond and Schwarz specimens in the transversal direction relative to the L-PBF building direction.

porosity, the EAS increases. This is confirmed here with the F_2CC_z structures having a significantly higher level of porosity of 90% compared to the 60% porous TPMS from the current study. The presence of vertical struts in the F_2CC_z lattices is also likely a contributing factor to the higher EAS, as they provide additional strength to bear the uni-axial compressive loads.

Based on the compressive mechanical properties of the Ti-25Ta lattices explored in this study, the diamond and gyroid unit-cell geometries are preferable for use as load-bearing bone implants, as the Schwarz primitive structure exhibited mechanical instability due to the presence of thin struts aligned with the loading direc-

tion. The Young's moduli for all lattice groups fall within the recommended range for use in cortical bone implant applications (i.e. 1–30 GPa [56]). For the gyroid and diamond unit-cells, it is possible to both increase or decrease the level of porosity and tailor the mechanical properties to attain a better biomechanical compatibility with the surrounding tissue.

The mechanical testing data also suggests that the unmelted Ta particles remaining in the materials have no significant influence on the quasi-static mechanical performances. Previous work has shown that the reduction in unmelted Ta through remelt scan strategies did not significantly improve fatigue lifetimes of dense
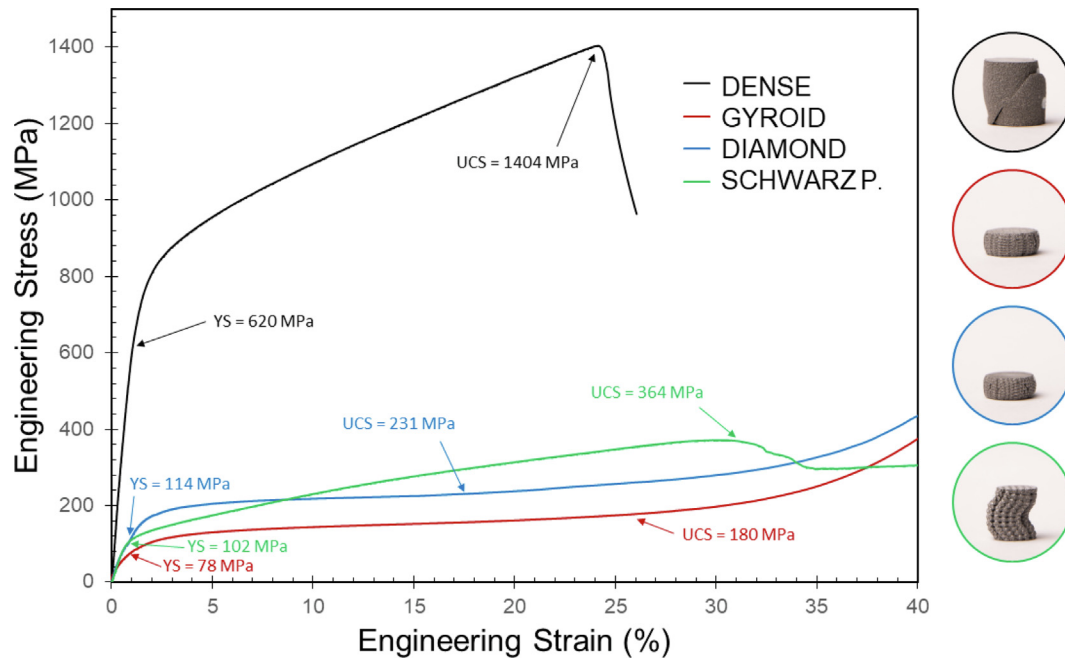
Fig. 6. Representative engineering stress–strain curves from the Ti-25Ta samples in uni-axial compression testing and their corresponding failure modes. Note that the yield strengths (YS) and ultimate compressive strengths (UCS) presented here correspond to only one specimen of each group. The averaged values for each groups with standard deviations are presented in Table 6.

Table 6
Compressive mechanical properties of the Ti-25Ta samples extracted from the compression tests and from similar materials reported in the literature.

Group ref.	Material	Lattice geometry	Designed Porosity (%)	Young's Modulus (GPa)	Yield Strength at 0.2% (MPa)	Ultimate Compressive Strength (MPa)	Specific Strength [a] (MPa)	Strain at Failure (%)	EAS [b] (%)	Reference
D	Ti-25Ta	N/A	0	70.3 ± 5.2	682 ± 55	1458 ± 212	1458	32 ± 10	0.97	This Work
G60	Ti-25Ta	Gyroid	60	10.4 ± 1.5	74 ± 4	171 ± 8	332	> 70[c]	0.72	This Work
D60	Ti-25Ta	Diamond	60	15.8 ± 0.5	126 ± 11	236 ± 6	340	> 70[c]	0.80	This Work
S60	Ti-25Ta	Schwarz p.	60	18.9 ± 2.0	102 ± 9	371 ± 56	741	26 ± 8	0.54	This Work
N/A	Ti-25Ta	Schwarz p.	64	14.3 ± 7.0	86 ± 7	N/A	N/A	> 70	0.60	[23]
N/A	Ti-25Ta	F_2CC_Z	90	1.96 ± 0.04	71 ± 2	101 ± 2	≈ 337	≥ 30	3.48	[52]
N/A	Ti-65Ta	F_2CC_Z	90	1.73 ± 0.03	62 ± 2	88 ± 3	≈ 293	≥ 30	3.24	[52]
N/A	Ti-25Ta	N/A	0	73.5 ± 1.8	620 ± 27	N/A	N/A	> 70	0.84	[23]
N/A	Ti-25Ta	N/A	0	65 ± 5	426 ± 14	N/A	N/A	25 ± 1	0.66	[24]
N/A	Ti-50Ta [d]	N/A	0	76 ± 4	883	N/A	N/A	12	1.16	[12]
N/A	Ti-6Al-4 V [d]	Gyroid	69	13.3	81	N/A	N/A	6.7	0.61	[55]
N/A	Cortical Bone	N/A	N/A	≈ 12.5	110	130	N/A	N/A	0.88	[56]

[a] The Specific Strength is defined by the UCS divided by the measured relative density (presented in Table 5).
[b] EAS is the elastic admissible strain defined by Eq(1).
[c] The strain at failure for the gyroid and diamond could not be measured as the tests were manually stopped at 70% strain.
[d] Data obtained from tensile test.

specimens [32] or lattices [57]. Rather, internal porosity or surface irregularities were the primary cause for crack initiation sites. In contrast to bulk material, lattices are more sensitive to surface irregularities than internal defects with respect to fatigue crack initiation sites [55]. This suggests that the unmelted Ta within the struts may not affect fatigue lifetimes. However, given the large amount of Ta particles located near the external surfaces (cf. Fig. 5), potential adverse effects may arise due to the combined impacts from the significant surface irregularities and abundant close-to-surface Ta particles. Future work could focus on in-

depth fatigue studies on Ti-25Ta TPMS lattices produced from elemental powder blends using L-PBF processes.

Fig. 7 presents the results from the FE models after applying a displacement of 0.15 mm (i.e. 5% strain) to the representative $3 \times 3 \times 3$ structures. The data shows that the G60 and S60 groups demonstrated comparable elastic moduli between the FEM and experimental data and a similar yield strength of 84 MPa was also observed for the gyroid group. Although presenting similar yield points, the yielding transitions for the S60_FEM and S60_EXP exhibit high variations. Because of the simple nature of the FE models
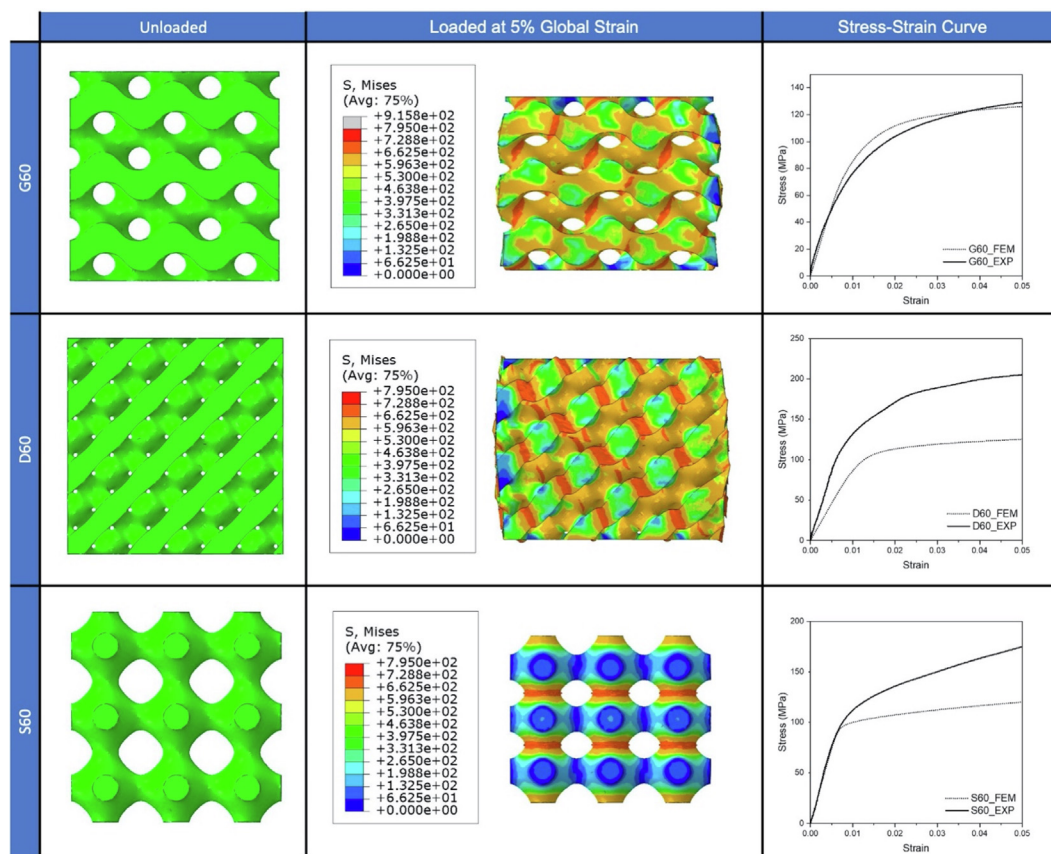
Fig. 7. Numerical study using the finite element method (FEM) and ABAQUS solver for a 5% global compression test and comparison with experimental tests.

(i.e. linear static), the buckling-like behavior of the Schwarz lattices is not captured in the numerical study. This likely explains the discrepancies in yielding transition for the Schwarz lattice group.

For the diamond lattices, the FE model underestimates the elastic modulus and yield strength by approximately 42% and 21% respectively, indicating that the fabricated D60 specimens were not representative of the designed lattices and that the manufacturing mismatch for this group had structural implications, in contrast to the mechanically insignificant surface irregularities due to semi-melted powder commonly observed with L-PBF [43].

The FEA results indicate that the processing of the Ti-25Ta lattices is consistent with the bulk material behavior for the gyroid and Schwarz primitive lattices. However, for the diamond lattices, the data indicates that the higher relative error in strut size between the CAD and actual fabricated specimens (cf. Fig. 4) has a large impact on resulting mechanical properties. The morphological mismatches discussed before can be directly correlated to the technical limitations involved with the fabrication of this specific D60 lattice design using L-PBF processing and this Ti-25Ta elemental powder blend. Improvements could be made by optimizing scanning strategy parameters (i.e. change in beam compensation and/or change in local scanning speeds for down-skin surfaces for instance) but a revised version of the lattice design may be a more effective and simpler way to overcome these limitations.

3.3. In vitro cell culture

The permeability of scaffolds and other three-dimensional constructs used for tissue engineering applications controls the diffusion of nutrients in and waste out of the scaffolds and hence influences the pressure fields within the construct. Pore structure

is an essential consideration in the development of scaffolds for bone tissue engineering. Pores must be interconnected to allow for cell in-growth, migration and nutrient flow. If pores are too small, cell migration is limited, resulting in the formation of a cellular capsule around the edges of the scaffold [41]. This in turn can limit diffusion of nutrients and removal of waste resulting in necrotic regions within the construct.

In the present study, the metabolic activity, proliferation, and attachment of osteoblast cells at 6, 24 and 72 h were investigated by AlamarBlue, PicoGreen and laser confocal microscopy (Fig. 8). Osteoblast cells showed a slight increase of metabolic activity after 24 h of culture compared to 6 h, for all samples, with no significant differences between sample geometries. After 72 h of culture, the lattices showed a higher metabolic activity compared to the dense samples (D group). The differences observed in number of attached cells at the early seeding time of 6 h (Fig. 8.b) notably highlights the differences in exposed surface area for each group. The dense specimens had the largest surface area and naturally shows the highest cell count at 6 h, followed by the Schwarz, the gyroid and the diamond. At 24 h, all groups showed an increase in cell count, with the dense specimens and Schwarz specimens having the smallest fold increases of 1.34 and 1.19 respectively, whereas the diamond group had the highest fold increase of 4.54 followed by the gyroid at 3.41. These measures indicate that the addition of an interconnected porous network to the Ti-25Ta alloy is advantageous for cell growth but also that the large pore size of the S60 group may not be favourable at short seeding times. However, at the longer seeding time (72 h), the S60 group showed the highest number of attached cells, with also the highest increase from the earlier seeding time of 24 h. This suggests that the larger pore size from the S60 group allows high cell migration and spreading at
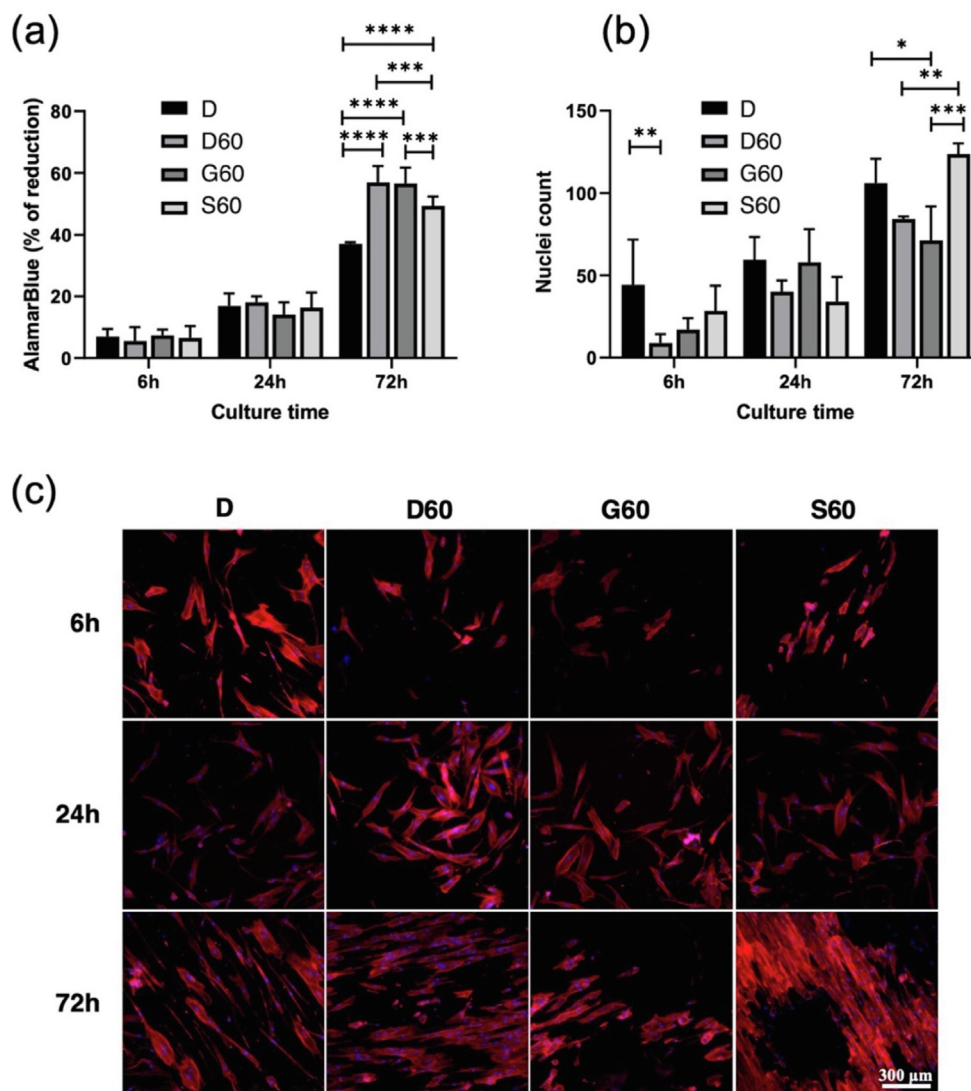
Fig. 8. (a) Metabolic activity measured by Alamar Blue, (b) DNA quantification by PicoGreen (c) Confocal images of the DAPI (nucleus, blue) and phalloindin (actin, red) staining with the Ti-25Ta scaffolds. (For interpretation of the references to colour in this figure legend, the reader is referred to the web version of this article.)

longer seeding times. Laser confocal microscopy images (Fig. 8.c) were in good agreement with the number of cells attached on the dense specimens and lattice groups. On the confocal images, the cells appeared to form a dense filamentous pattern for the S60 group, and formed in layers surrounding the pores, rather than a scattered formation as observed for the other groups. Due to the uncertainty associated with the cut location from the protocol, the differences in surface areas exposed likely contribute to these observations and to the measured cell activity. For instance, the Schwarz specimens would in theory have larger initial metabolic activity when cut at its thickest section with higher surface area exposed. Thus, further studies should focus on the effect of pore shape, size and surface areas on metabolic activity specifically.

4. Conclusion

The manufacture of bio-mimetic bone scaffolds based on minimal surfaces with L-PBF using a titanium-tantalum pre-mixed alloy has been successfully demonstrated in this work. The resulting compressive mechanical properties of the lattice structures are shown to be suitable for bone tissue engineering applications, and the topological features of the designed TPMS lattices are retained through the processing, although substantial surface irregularities are present, and unmelted Ta particles remained within the Ti-Ta matrix. The following conclusions can be drawn from the study:

(i) The topologies from the TPMS equations were retained in the L-PBF processing and the fabricated gyroid, diamond and Schwarz primitive lattices showed a similar increase in strut sizes of approximately 110 μm compared to their CAD equivalents. To prevent pore obstructions from semi-molten excess material, it is recommended that small pore sizes of 400 μm and below should be avoided in the design phase.

(ii) The proportion of remaining unmelted Ta particles within the Ti-Ta matrix were found to be higher in the lattices (6.1%) than in the dense specimens (2.1%). This was attributed to the reduction in heat exposure and energy density in lattices' struts compared to dense material during processing. Furthermore, the unmelted Ta particles presented a heterogeneous distribution within the struts, with higher density towards the surfaces of the lattices, where heat exposure is further reduced.

(iii) The use of TPMS for tailoring the mechanical properties of metallic biomaterials was shown to be successful through this work. All lattices presented adequate mechanical properties for use as biomedical replacement implants, with an average EAS of 0.69 and high ductility. However, the Schwarz lattices consistently failed under buckling, which highlighted the instability of the structure due to the alignment of thin vertical struts with the loading direction. The G60 and D60 designs are thus preferable for load-bearing applications due their better stability and high ductility.

(iv) The cell culture tests demonstrated the excellent biocompatibility of the Ti-25Ta lattices and their superior biological response in comparison to the dense Ti-25Ta. The Schwarz lattices showed higher metabolic activity compared to the gyroid and diamond, but further studies would be required to understand the effect of pore shape, size and associated surface areas on metabolic activity.

Declaration of Competing Interest

The authors declare that they have no known competing financial interests or personal relationships that could have appeared to influence the work reported in this paper.

Acknowledgments

References

[1] C.G.S. Anwar et al., Finite element analysis of porous medical grade cobalt chromium alloy structures produced by selective laser melting, Advanced Materials Research 1133 (2016) 113–118.

[2] L. Mullen, R.C. Stamp, W.K. Brooks, E. Jones, C.J. Sutcliffe, Selective Laser Melting: A regular unit cell approach for the manufacture of porous, titanium, bone in-growth constructs, suitable for orthopedic applications, Journal of Biomedical Materials Research Part B: Applied Biomaterials 89B (2) (2009) 325–334.

[3] B. Vandenbroucke, J.-P. Kruth, Selective laser melting of biocompatible metals for rapid manufacturing of medical parts, Rapid Prototyping Journal 13 (4) (2007) 196–203.

[4] S. Van Bael, G. Kerckhofs, M. Moesen, G. Pyka, J. Schrooten, J.-P. Kruth, Micro-CT-based improvement of geometrical and mechanical controllability of selective laser melted Ti6Al4V porous structures, Materials Science and Engineering: A 528 (24) (2011) 7423–7431.

[5] N. Taniguchi, S. Fujibayashi, M. Takemoto, K. Sasaki, B. Otsuki, T. Nakamura, T. Matsushita, T. Kokubo, S. Matsuda, Effect of pore size on bone ingrowth into porous titanium implants fabricated by additive manufacturing: an in vivo experiment, Materials Science and Engineering: C 59 (2016) 690–701.

[6] C. Yan, L. Hao, A. Hussein, P. Young, Ti–6Al–4V triply periodic minimal surface structures for bone implants fabricated via selective laser melting, journal of the mechanical behavior of biomedical materials 51 (2015) 61–73.

[7] L. Zhang, G. Yang, B.N. Johnson, X. Jia, Three-dimensional (3D) printed scaffold and material selection for bone repair, Acta biomaterialia 84 (2019) 16–33.

[8] A. Ataee, Y. Li, M. Brandt, C. Wen, Ultrahigh-strength titanium gyroid scaffolds manufactured by selective laser melting (SLM) for bone implant applications, Acta Materialia 158 (2018) 354–368.

[9] C. Han, Y. Li, Q. Wang, S. Wen, Q. Wei, C. Yan, L. Hao, J. Liu, Y. Shi, Continuous functionally graded porous titanium scaffolds manufactured by selective laser melting for bone implants, Journal of the mechanical behavior of biomedical materials 80 (2018) 119–127.

[10] N. Soro, N. Saintier, H. Attar, M.S. Dargusch, Surface and morphological modification of selectively laser melted titanium lattices using a chemical post treatment, Surface and Coatings Technology 393 (2020) 125794.

[11] S. L. Sing, "Selective laser melting of novel titanium-tantalum alloy as orthopaedic biomaterial," 2016.

[12] S.L. Sing, W.Y. Yeong, F.E. Wiria, Selective laser melting of titanium alloy with 50 wt% tantalum: Microstructure and mechanical properties, Journal of Alloys and Compounds 660 (2016) 461–470.

[13] A. Cheng, A. Humayun, D.J. Cohen, B.D. Boyan, Z. Schwartz, Additively manufactured 3D porous Ti-6Al-4V constructs mimic trabecular bone structure and regulate osteoblast proliferation, differentiation and local factor production in a porosity and surface roughness dependent manner, Biofabrication 6 (4) (2014) 045007.

[14] P. Heinl, A. Rottmair, C. Körner, R.F. Singer, Cellular titanium by selective electron beam melting, Advanced Engineering Materials 9 (5) (2007) 360–364.

[15] M. Niinomi, M. Nakai, Titanium-Based Biomaterials for Preventing Stress Shielding between Implant Devices and Bone, International Journal of Biomaterials 2011 (2011) 1–10.

[16] Y. Zhang, P. Xiu, Z. Jia, T. Zhang, C. Yin, Y. Cheng, H. Cai, K.e. Zhang, C. Song, H. Leng, W. Yuan, Z. Liu, Effect of vanadium released from micro-arc oxidized porous Ti6Al4V on biocompatibility in orthopedic applications, Colloids and Surfaces B: Biointerfaces 169 (2018) 366–374.

[17] C.N. Elias, J.H.C. Lima, R. Valiev, M.A. Meyers, Biomedical applications of titanium and its alloys, Jom 60 (3) (2008) 46–49.

[18] G. He, M. Hagiwara, Ti alloy design strategy for biomedical applications, Materials Science and Engineering: C 26 (1) (2006) 14–19.

[19] M.T. Mohammed, Development of a new metastable beta titanium alloy for biomedical applications, Karbala International Journal of Modern Science 3 (4) (2017) 224–230.

[20] R. Wauthle, J. van der Stok, S. Amin Yavari, J. Van Humbeeck, J.-P. Kruth, A.A. Zadpoor, H. Weinans, M. Mulier, J. Schrooten, Additively manufactured porous tantalum implants, Acta biomaterialia 14 (2015) 217–225.

[21] V.K. Balla, S. Bose, N.M. Davies, A. Bandyopadhyay, Tantalum—A bioactive metal for implants, Jom 62 (7) (2010) 61–64.

[22] R. Wauthlé, J.-P. Kruth, M. Montero, L. Thijs, J. Van Humbeeck, New opportunities for using tantalum for implants with Additive Manufacturing, Eur Cells Mater 26 (2013) 15.

[23] N. Soro, H. Attar, E. Brodie, M. Veidt, A. Molotnikov, M.S. Dargusch, Evaluation of the mechanical compatibility of additively manufactured porous Ti–25Ta alloy for load-bearing implant applications, Journal of the mechanical behavior of biomedical materials 97 (2019) 149–158.

[24] E. Brodie, A. Medvedev, J. Frith, M. Dargusch, H. Fraser, A. Molotnikov, Remelt processing and microstructure of selective laser melted Ti25Ta, Journal of Alloys and Compounds 820 (2020) 153082.

[25] J. Matena et al., SLM produced porous titanium implant improvements for enhanced vascularization and osteoblast seeding, International journal of molecular sciences 16 (4) (2015) 7478–7492.

[26] F.S.L. Bobbert, K. Lietaert, A.A. Eftekhari, B. Pouran, S.M. Ahmadi, H. Weinans, A. A. Zadpoor, Additively manufactured metallic porous biomaterials based on minimal surfaces: A unique combination of topological, mechanical, and mass transport properties, Acta Biomaterialia 53 (2017) 572–584.

[27] S. Maietta, A. Gloria, G. Improta, M. Richetta, R. De Santis, M. Martorelli, A Further Analysis on Ti6Al4V Lattice Structures Manufactured by Selective Laser Melting, Journal of Healthcare Engineering 2019 (2019) 1–9.

[28] E. Alabort, D. Barba, R.C. Reed, Design of metallic bone by additive manufacturing, Scripta Materialia 164 (2019) 110–114.

[29] S. Van Bael et al., The effect of pore geometry on the in vitro biological behavior of human periosteum-derived cells seeded on selective laser-melted Ti6Al4V bone scaffolds, Acta biomaterialia 8 (7) (2012) 2824–2834.

[30] S. Ozan, J. Lin, Y. Li, R. Ipek, C. Wen, Development of Ti–Nb–Zr alloys with high elastic admissible strain for temporary orthopedic devices, Acta biomaterialia 20 (2015) 176–187.

[31] E.G. Brodie, K.J. Robinson, E. Sigston, A. Molotnikov, J.E. Frith, Osteogenic Potential of Additively Manufactured TiTa Alloys, ACS Applied Bio Materials 4 (1) (2021) 1003–1014.

[32] E.G. Brodie, J. Richter, T. Wegener, T. Niendorf, A. Molotnikov, Low-cycle fatigue performance of remelted laser powder bed fusion (L-PBF) biomedical Ti25Ta, Materials Science and Engineering: A 798 (2020) 140228.

[33] L. Haferkamp, S. Liechti, A. Spierings, K. Wegener, Effect of bimodal powder blends on part density and melt pool fluctuation in laser powder bed fusion, Progress in Additive Manufacturing 6 (3) (2021) 407–416.

[34] H. Chen, Q. Wei, Y. Zhang, F. Chen, Y. Shi, W. Yan, Powder-spreading mechanisms in powder-bed-based additive manufacturing: Experiments and computational modeling, Acta Materialia 179 (2019) 158–171.

[35] O. Al-Ketan, R. Rowshan, R.K. Abu Al-Rub, Topology-mechanical property relationship of 3D printed strut, skeletal, and sheet based periodic metallic cellular materials, Additive Manufacturing 19 (2018) 167–183.

[36] T. Hildebrand, P. Rüegsegger, A new method for the model-independent assessment of thickness in three-dimensional images, Journal of microscopy 185 (1) (1997) 67–75.

[37] G. Abaqus, "Abaqus 6.11," *Dassault Systemes Simulia Corporation, Providence, RI, USA,* 2011.

[38] H. Jiang, H. Ziegler, Z. Zhang, H. Meng, D. Chronopoulos, Y. Chen, Mechanical properties of 3D printed architected polymer foams under large deformation, Materials & Design 194 (2020) 108946.

[39] B. Lozanovski et al., Computational modelling of strut defects in SLM manufactured lattice structures, Materials & Design 171 (2019) 107671.

[40] H. Haase, S. Ivanovski, M. Waters, P. Bartold, Growth hormone regulates osteogenic marker mRNA expression in human periodontal fibroblasts and alveolar bone-derived cells, Journal of periodontal research 38 (4) (2003) 366–374.

[41] A. Abdal-hay, N.T. Raveendran, B. Fournier, S. Ivanovski, Fabrication of biocompatible and bioabsorbable polycaprolactone/magnesium hydroxide 3D printed scaffolds: Degradation and in vitro osteoblasts interactions, Composites Part B: Engineering 197 (2020) 108158.

[42] S. Arabnejad, R. Burnett Johnston, J.A. Pura, B. Singh, M. Tanzer, D. Pasini, High-strength porous biomaterials for bone replacement: A strategy to assess the interplay between cell morphology, mechanical properties, bone ingrowth and manufacturing constraints, Acta biomaterialia 30 (2016) 345–356.

[43] N. Soro, H. Attar, X. Wu, M.S. Dargusch, Investigation of the structure and mechanical properties of additively manufactured Ti-6Al-4V biomedical scaffolds designed with a Schwartz primitive unit-cell, Materials Science and Engineering: A 745 (2019) 195–202.

[44] J. Sienkiewicz, P. Płatek, F. Jiang, X. Sun, A. Rusinek, Investigations on the mechanical response of gradient lattice structures manufactured via SLM, Metals 10 (2) (2020) 213.

[45] V. Deshpande, M. Ashby, N. Fleck, Foam topology: bending versus stretching dominated architectures, Acta materialia 49 (6) (2001) 1035–1040.

[46] D. Pihler-Puzović, A. Hazel, T. Mullin, Buckling of a holey column, Soft Matter 12 (34) (2016) 7112–7118.

[47] A. Nazir, A.B. Arshad, J.-Y. Jeng, Buckling and post-buckling behavior of uniform and variable-density lattice columns fabricated using additive manufacturing, Materials 12 (21) (2019) 3539.

[48] K.C. Nune, A. Kumar, R.D.K. Misra, S.J. Li, Y.L. Hao, R. Yang, Functional response of osteoblasts in functionally gradient titanium alloy mesh arrays processed by 3D additive manufacturing, Colloids and Surfaces B: Biointerfaces 150 (2017) 78–88.

[49] A. Ataee, Y. Li, D. Fraser, G. Song, C. Wen, Anisotropic Ti-6Al-4V gyroid scaffolds manufactured by electron beam melting (EBM) for bone implant applications, Materials & Design 137 (2018) 345–354.

[50] R.S. Bonatti, Y.A. Meyer, A.D. Bortolozo, D. Costa, W.R. Osório, Morphology and size effects on densification and mechanical behavior of sintered powders from Al-Si and Al-Cu casting alloys, Journal of Alloys and Compounds 786 (2019) 717–732.

[51] Y.A. Meyer, R.S. Bonatti, D. Costa, A.D. Bortolozo, W.R. Osorio, Compaction pressure and Si content effects on compressive strengths of Al/Si/Cu alloy composites, Materials Science and Engineering: A 770 (2020) 138547.

[52] E.G. Brodie, T. Wegener, J. Richter, A. Medvedev, T. Niendorf, A. Molotnikov, A mechanical comparison of alpha and beta phase biomedical TiTa lattice structures, Materials & Design 212 (2021) 110220, https://doi.org/10.1016/j.matdes.2021.110220.

[53] M. Benedetti, J. Klarin, F. Johansson, V. Fontanari, V. Luchin, G. Zappini, A. Molinari, Study of the compression behaviour of Ti6Al4V trabecular structures produced by additive laser manufacturing, Materials 12 (9) (2019) 1471, https://doi.org/10.3390/ma12091471.

[54] X. Zheng, Z. Fu, K. Du, C. Wang, Y. Yi, Minimal surface designs for porous materials: from microstructures to mechanical properties, Journal of materials science 53 (14) (2018) 10194–10208.

[55] N. Soro, N. Saintier, J. Merzeau, M. Veidt, M.S. Dargusch, Quasi-static and fatigue properties of graded Ti–6Al–4V lattices produced by Laser Powder Bed Fusion (LPBF), Additive Manufacturing 37 (2021) 101653.

[56] J. R. Jameson, "Characterization of bone material properties and microstructure in osteogenesis imperfecta/brittle bone disease," Marquette University, 2014.

[57] B. ERIN GRACE, *Additively Manufactured TiTa Alloys for Improved Osseointegration of Bone Implants.* 2020.